

Detecting Atlantic MOC Changes in an Ensemble of Climate Change Simulations

S. S. DRIJFHOUT AND W. HAZELEGER

Royal Netherlands Meteorological Institute (KNMI), De Bilt, Netherlands

(Manuscript received 21 June 2006, in final form 14 August 2006)

ABSTRACT

Signal-to-noise patterns for the meridional overturning circulation (MOC) have been calculated for an ensemble of greenhouse scenario runs. The greenhouse-forced signal has been defined as the linear trend in ensemble-mean MOC, after year 2000. It consists of an overall decrease and shoaling of the MOC, with maximum amplitudes of 10 Sv ($\text{Sv} \equiv 10^6 \text{ m}^3 \text{ s}^{-1}$) per century. In each member the internal variability is defined as the anomaly with respect to the ensemble-mean signal. The interannual variability of the MOC is dominated by a monopole with a maximum amplitude of 2 Sv at 40°N. This variability appears to be driven by the North Atlantic Oscillation (NAO), mainly through NAO-induced variations in the wind field.

The signal-to-noise ratio was estimated for various time spans, all starting in 1950 or later. Different noise estimates were made, both with and without intra-annual variability, relevant for episodic and continuous monitoring, respectively, and with and without an estimate of the observational error. Detection of a greenhouse-forced MOC signal on the basis of episodic measurements is impossible before 2055. With continuous monitoring, detection becomes possible after 35 years of observation. The main motivation for calculating signal-to-noise ratios and detection times is their usefulness for local monitoring strategies and detection methods. The two-dimensional pattern of detection times of a MOC change supports the rationale for deploying a sustained monitoring array on at 26°N.

1. Introduction

The Atlantic meridional overturning circulation (MOC) is associated with a large northward heat flux: north of 30°N, the MOC dominates global ocean heat transport (Ganachaud and Wunsch 2000). As a result, the MOC has a substantial influence on the climate of the Northern Hemisphere. A weakening, or even collapse, of the Atlantic MOC [in particular that part that is associated with the southward flow of North Atlantic Deep Water (NADW) and its northward, shallow return flow] might lead to significant cooling over the North Atlantic and northwestern Europe (e.g., Manabe and Stouffer 1994; Vellinga and Wood 2002).

Since the work of Stommel (1961) it is known that thermohaline flows may possess multiple equilibria and hysteresis behavior. Although one might question to what extent the Atlantic MOC is a “thermohaline” circulation (Wunsch 2002), several ocean general circulation models (OGCMs), have recovered the collapsed

state of the MOC (e.g., Manabe and Stouffer 1988; Mikolajewicz and Maier-Reimer 1994; Rahmstorf et al. 2005). Many modeling studies suggest a marked sensitivity of the MOC to anthropogenic climate change (Gregory et al. 2005), and because of its strong nonlinearity, a rapid, substantial reorganization of the MOC appears to be possible (Rahmstorf 1995).

Most models predict, as a response to greenhouse gas (GHG) forcing, a MOC decrease (e.g., Dixon et al. 1999; Mikolajewicz and Voss 2000; Thorpe et al. 2001; Gregory et al. 2005), but no consensus has emerged regarding the principal feedback that determines the response of the MOC to anthropogenic forcing. Latif et al. (2000), for instance, discuss a tropical feedback that stabilizes the MOC in response to anthropogenic forcing. Although a transient weakening is the most common response of the MOC to greenhouse forcing, to date there is no published climate scenario run that simulates a collapse of the MOC before the year 2100. Anthropogenic climate change, however, might very well move the MOC toward the bifurcation point beyond which NADW formation ceases to exist. At least, this is suggested by the $4 \times \text{CO}_2$ run discussed by Manabe and Stouffer (1999) in which the MOC remains in a collapsed state for several ages. Some present-day

Corresponding author address: S. S. Drijfhout, Royal Netherlands Meteorological Institute (KNMI), P.O. Box 201, 3730 AE De Bilt, Netherlands.
E-mail: drijfhou@knmi.nl

climate models seem to drift away from the (possible) bifurcation point, displaying a much too stable MOC in association with a too evaporative Atlantic basin (Pardaens et al. 2003). It is likely that, in case of such a drift, these models underestimate the response of the MOC to enhanced greenhouse forcing.

Bryden et al. (2005) report a slowing of the MOC over the past 50 years that is associated with a much stronger trend than nearly any model integrated with realistically increasing greenhouse concentrations has been able to simulate (Gregory et al. 2005). The MOC decrease reported by Bryden et al., however, may be severely biased by undersampled natural variability of the MOC. This is extensively discussed by Wunsch and Heimbach (2006). Before detection of a change can be made, one must first be able to estimate whether the change is associated with a real trend or whether it represents a fluctuation that results from the internal variability. Such a more complete analysis, with separate estimates of the “signal” and “noise,” was performed by Baehr et al. (2007) in a numerical model for the U.K./U.S. Rapid Climate Change/Western Atlantic Variability Experiment (RAPID/WAVE) 26°N array.

In the following, we address the question of detecting trends in the MOC by analyzing a large (62) ensemble of climate model simulations, all forced with increasing levels of greenhouse gas concentrations in the atmosphere. With the aid of such a large ensemble, the forced signal and internal variability can be separated from each other and described more robustly than is possible with only a few runs. We simply assume that the forced signal is contained in the ensemble-mean average. Then, the internal variability in each individual ensemble member is defined as the anomaly with respect to the ensemble-mean signal. This definition allows for a complete description of the temporal and spatial character of both signal and noise. Also, it allows for an estimate of the detection time, being the time at which the signal-to-noise ratio exceeds a critical level. The main motivation for calculating these signal-to-noise ratios is their usefulness for in situ monitoring strategies and detection methods.

2. The ensemble experiment

The model used for this study is version 1.4 of the Community Climate System Model (CCSM) of the National Center for Atmospheric Research. It simulates the evolution of the coupled atmosphere–ocean–sea ice–land system under prescribed climate forcing. The atmosphere was run with a spectral resolution of T31 and 18 levels in the vertical. The land model distinguishes between specified vegetation types and contains a comprehensive treatment of surface processes.

The sea ice model includes ice thermodynamics and dynamics. The ocean model has 25 vertical levels and a 3.6° longitudinal resolution. The latitudinal resolution ranges from 0.9° in the Tropics to 1.8° at higher latitudes. The coupled system does not require artificial flux corrections to simulate a realistic climate (Boville et al. 2001).

The simulations cover the period 1940–2080. Until 2000, the forcing includes specified estimates of temporally evolving solar radiation, temporally and geographically dependent aerosols due to manmade and natural emissions, and time-dependent GHGs. From 2000 onward all forcings are kept at the 2000 values, except for the concentration of GHGs, which increase according to a “business-as-usual” (BAU) scenario. This BAU scenario closely follows the Special Report on Emissions Scenarios (SRES) A1 scenario and CO₂ concentrations increase to 640 ppmv by 2080, the end of the simulation period (Dai et al. 2001). For more details on the model and on the ensemble experiment we refer to Boville et al. (2001) and Selten et al. (2004), respectively.

An ensemble of 62 simulations was produced, each covering a 140-yr period. The simulations differ only in a small random perturbation to the initial atmospheric temperature field, which leads, due to the chaotic nature of the atmospheric flow, to completely different weather patterns by the end of the first month. After a few years of spinup, the ocean circulation in each ensemble member has become decoupled from its initial state. Averaging over all ensemble members filters out most of the internally generated climate variations and allows for an estimate of the externally forced climate signal. Also, by analyzing the detrended time series of all ensemble members the internal variability can be much more adequately described than is possible for a single climate-scenario run.

In the following, we will disregard the first 10 years of each integration to allow the ocean circulation in each ensemble member to become decoupled from its common initial state. For this reason, our analysis will start in 1950 instead of 1940.

3. Response to anthropogenic forcing: The forced signal

The complete MOC in the Atlantic consists of several overturning cells. However, it is dominated by one basinwide cell that is associated with the southward flow of NADW and a compensating, shallower return flow. It is this single overturning cell that appears most sensitive to anthropogenic forcing and that can be associated with possibly nonlinear behavior. For simplic-

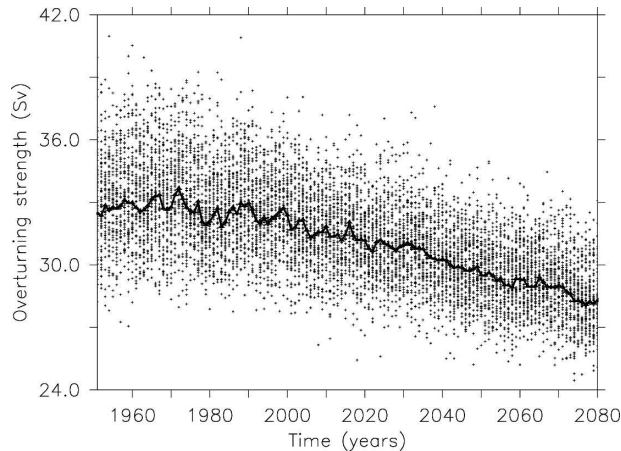


FIG. 1. The ensemble-averaged maximum overturning as a function of time (thick black line) showing the response of the MOC to GHG forcing since 1950, together with the 62 ensemble members (dots) showing the spread due to internal variability (in Sv).

ity, in the remainder of the text we will identify the Atlantic MOC with this single overturning cell.

Figure 1 shows the ensemble-mean, yearly averaged maximum overturning as a function of time, showing the response of the MOC to GHG forcing since 1950, together with the 62 ensemble members showing the spread due to the yearly averaged internal variability. In the early phase the MOC seems to equilibrate at a peak value of about 33 Sverdrup ($\text{Sv} \equiv 10^6 \text{ m}^3 \text{ s}^{-1}$), and this overturning level is maintained until the year 2000. The following 80 years (2000–80) show an almost linear decrease. The overall decrease of maximum overturning is about 5–6 Sv.

With a peak value of 33 Sv at 40°N , the MOC is definitely too strong, although 23-Sv outflow at 30°S comes closer to observational estimates (e.g., Ganachaud and Wunsch 2000). Despite the use of isopycnal mixing (Gent and McWilliams 1990), there is a lot of upwelling in the North Atlantic associated with a 10-Sv overturning cell between 10° and 50°N , which seems unrealistic. Although there appears to be a bias in the ensemble-mean overturning circulation, the response to enhanced greenhouse forcing compares well with estimates from other models, in particular those that display a more realistic MOC (Gregory et al. 2005). In Gregory et al. a comparison is made between models that have run a transient integration with a $1\% \text{ yr}^{-1}$ increase of CO_2 concentration for a period of 140 yr. If we take the more realistic overturning maximum of 20 Sv, the expected decrease would be $6.5 \text{ Sv century}^{-1}$, quite comparable to the 5–6-Sv decrease we find in the period 2000–80 for the present model. Also, the bias in relative change is less compared to the results of

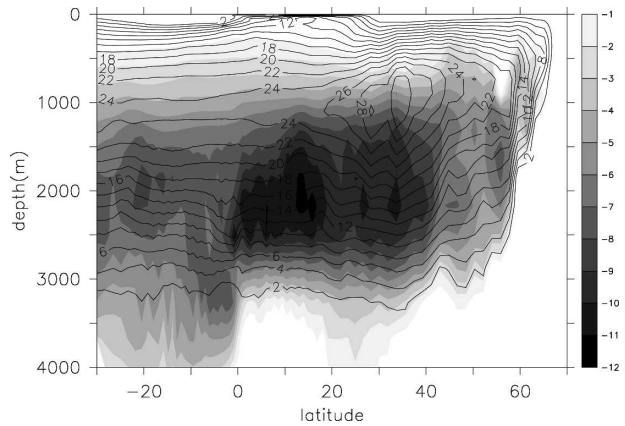


FIG. 2. The pattern of anthropogenically forced MOC change obtained by calculating the linear trend in ensemble-mean overturning for the period 2000–80. Units are $\text{Sv} (100 \text{ yr})^{-1}$. Only negative trends have been displayed. This pattern is overlaid by contours of the ensemble-mean meridional overturning for the year 2000.

Schmittner et al. (2005). They estimated a mean reduction of the MOC of 25% by 2100 from an ensemble of climate models, while the present model shows a reduction of 20%, if extended to 2100. So we conclude that overturning itself in the model is biased, but the absolute trend in overturning maximum, showing a somewhat weak relative change, is in good agreement with model estimates based on a more realistic overturning maximum of 20 Sv.

The linear trend in the ensemble-mean MOC for the period 2000–80 is shown in Fig. 2, together with a 10-yr average for the MOC at year 2000. The pattern associated with the decrease of the ensemble-mean MOC is a single meridional cell that extends over the full latitudinal range of the basin. South of 50°N , the MOC decreases almost uniformly. The largest decrease is found at about 2000-m depth where the trend is everywhere larger than $7 \text{ Sv} (100 \text{ yr})^{-1}$, with peak values of $11 \text{ Sv} (100 \text{ yr})^{-1}$ at 15°N . The maximum values in MOC change lie well below the level where the MOC itself peaks. This implies that the MOC not only decreases, but also shoals. Apparently the lightening of NADW caused by increased GHG forcing is larger than the lightening of Antarctic Bottom Water.

The shoaling of the MOC that we observe in response to increased GHGs has also been reported by Manabe and Stouffer (1994) in their transient runs during the time that the MOC was decreasing. Also Bryden et al. (2005) report a MOC decrease since 1957 in which the reduction of NADW outflow is completely confined to the deeper layer of 3000–5000 m, consistent with a shoaling MOC. The broad pattern associated with MOC decrease (Fig. 2) cannot be directly com-

pared with a comparable figure in the published literature, but it is consistent with the figures of an overall reduction or partial collapse of the MOC that have been published throughout the literature over the last years.

The zonally integrated picture of MOC decrease hides some marked zonal asymmetries. The decrease of the MOC is due to an almost complete cessation of deep-water formation in the Labrador and Irminger Seas. In the Greenland and Norwegian Seas, deep-water formation slightly increases and the formation region is shifted toward the northwest, producing a denser variety of NADW. The result that in response to increased GHGs convection in the western part of the subpolar gyre decreases much more rapidly than in the east was, for instance, also obtained by Wood et al. (1999). For more discussion on this change in deep-water formation, we refer to Drijfhout and Hazeleger (2006).

By and large, we conclude that the signal that we obtain from the ensemble of GHG simulations is realistic, as far as can be assessed from the sparse observations and other model experiments.

4. Internal variability

To detect anthropogenically forced changes in the MOC, a signal-to-noise ratio has to be established. In this problem the noise is defined by the internal variability. We start with discussing the interannual variability, as the longer time scales of the natural variability interact mostly with a long-term trend. Also, the interannual variability of the MOC has been widely discussed in the literature.

The first empirical orthogonal function (EOF) of interannual variability of the MOC, defined with respect to the ensemble-mean MOC, is a monopole with maximum amplitude at 30°N; north of 50°N the amplitude is almost zero. Also, the amplitude linearly decreases between 20°N and 30°S. This EOF explains 25.6% of the total variance. The second EOF is a dipole with opposite maxima at 30°N and 15°S, the northern cell being stronger. This EOF explains 13.5% of the variance. Both spectra of these EOFs are red, without any significant peak. Instead of showing the EOFs, we show the regression patterns of the time series of anomalous overturning (Fig. 3) and anomalous horizontal barotropic circulation (Fig. 4) on the detrended time series of overturning maximum, to elucidate the three-dimensional character of the mode. The pattern displayed in Fig. 3 strongly resembles EOF1, but it is more symmetric, with less variability in the Southern Hemisphere. The associated spectrum is somewhat less red than the

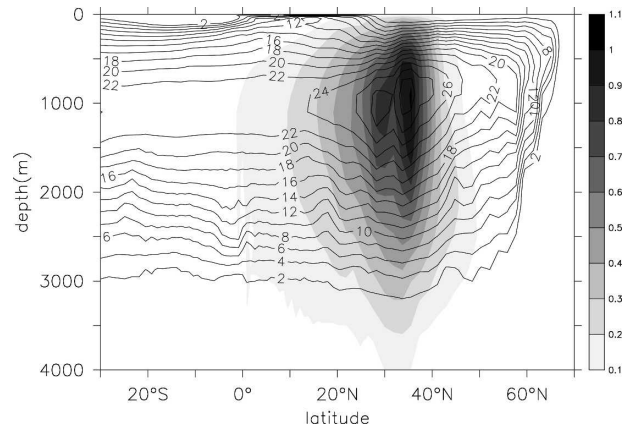


FIG. 3. Pattern of interannual variability of the MOC associated with variations in overturning strength. This pattern is obtained by a linear regression of the time series of anomalous overturning (overturning minus ensemble-mean overturning) on the detrended time series of overturning maximum (overturning maximum minus ensemble-mean overturning maximum). Units are nondimensional. It shows a monopole describing oscillations in overturning strength largely confined to the Northern Hemisphere. This pattern is overlaid by contours of the time-averaged ensemble-mean meridional overturning.

spectrum of EOF1, as it contains more high frequencies. There is no significant peak, but enhanced variability around the frequency bands of 5 and 20 yr. When low-pass time filtering is applied the pattern shown in Fig. 3 broadens and more closely resembles the pattern of EOF1. This can be explained as the equator effectively acts as a low-pass filter (see Johnson and Marshall 2002).

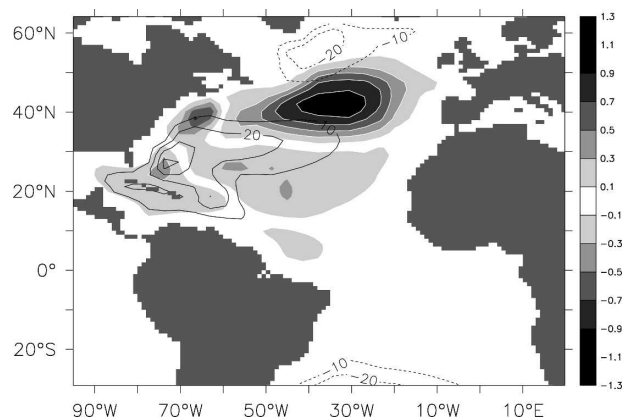


FIG. 4. Pattern of internal variability of the horizontal (barotropic) gyre that is associated with variations in overturning strength. This pattern is obtained by a linear regression of the time series of anomalous barotropic circulation on the detrended time series of overturning maximum. It is overlaid by contours of the ensemble-mean barotropic circulation. The pattern of variability is a di(tri)pole with positive values contoured in white.

Figure 4 shows the variability in barotropic gyre circulation associated with variations in maximum overturning. This pattern is nearly identical to the first EOF of barotropic gyre variability. The pattern is overlaid by contours of the mean barotropic circulation. The dominant mode of variability is characterized by a tripole with the most northern pole, which is centered across the eastern part of the midlatitude jet or subtropical/subpolar gyre boundary, being dominant. This pole reflects a simultaneous expansion (contraction) of the subtropical gyre and contraction (expansion) of the subpolar gyre. The expanding gyres also increase their strength. The correlation between the time series associated with the two patterns, shown in Figs. 3 and 4, is about 0.8.

When the overturning increases there is enhanced northward flow along the American coast (overshoot of the Gulf Stream) and enhanced southward return flow farther offshore. This pattern strongly projects on the vertical, with the southward return flow occurring below the northward flow in the western boundary current. When the overturning increases, the most southern pole indicates a decrease of the strength of the subtropical gyre and a northward shift of the eastward return flow. This pattern of variability resembles the ocean gyre circulation changes that occur in response to the North Atlantic Oscillation (NAO), as described by Curry and McCartney (2001), although details of the pattern differ.

Also in the present model, the dominant modes of variability in MOC and horizontal gyre circulation seem to be driven by the NAO. A linear regression of the time series of anomalous overturning on the NAO index yields patterns that strikingly resemble the patterns shown in Figs. 3 and 4. Figure 5 shows the pattern of MOC variability that is associated with the NAO. This pattern almost completely recovers the first EOF of the internal variability.

The MOC is thought to display an integrated response to the NAO (Eden and Willebrand 2001), implying that the regression between maximum overturning and NAO index might peak at a certain lag, especially when the NAO projects on the buoyancy forcing. In the present model, however, the regression peaks when the NAO leads with 1 yr. This result suggests that the overturning oscillation that we find is mainly responding to NAO-induced wind variations and that the NAO-induced buoyancy-forced response of the MOC is weaker.

Delworth et al. (1993) were the first to identify an interdecadal MOC oscillation in a globally coupled model. They did not show the associated MOC pattern since they focused on the variability of the maximum

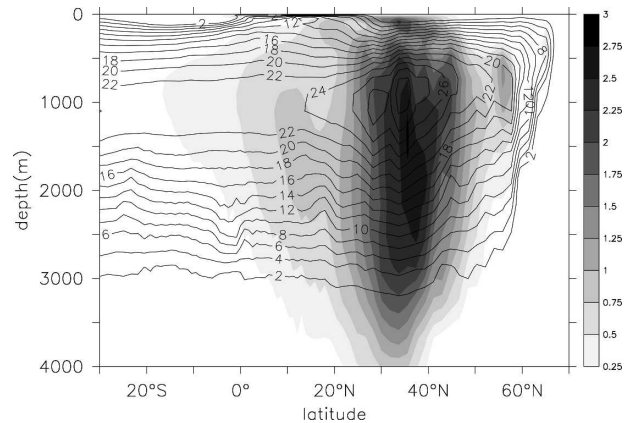


FIG. 5. Pattern of interannual variability of the MOC associated with variations in the NAO. This figure is obtained in a similar way as Fig. 3, but now a linear regression of the time series of anomalous overturning on the NAO index is performed. Units are mSv hPa^{-1} . This pattern strikingly resembles the pattern shown in Fig. 3.

MOC strength. But the oscillation that they describe can be associated with the main oscillatory mode that destabilizes buoyancy driven steady flows, which is characterized by a large monopole, with maximum amplitude at the location of maximum overturning strength (e.g., Dijkstra and Ghil 2005). Both Timmermann et al. (1998) and Dong and Sutton (2001) describe MOC oscillations that resemble monopoles, like the Delworth et al. (1993) oscillation. Eden and Willebrand (2001) find that the dominant oscillation has a dipole character. There is agreement on the prominent role of the NAO in association with MOC variability, but the associated ocean–atmosphere interaction differs among studies, ranging from the MOC being coupled to the low-frequency part of the NAO (Timmermann et al. 1998); excited by noise that is associated with the NAO (Delworth and Greatbatch 2000); forced by the low-frequency part of the NAO (Dong and Sutton 2001; Eden and Willebrand 2001).

In summary, both pattern and amplitude of interannual MOC variability (a variance of 4 Sv^2 [equal to $(2 \text{ Sv})^2$ squared: 4 Sv^2] for maximum overturning strength), as determined in the present model, seem realistic compared to other model estimates. Also, the strong relation between NAO and MOC variability reported by many other studies is recovered. From these studies we infer that no agreement has been reached on details about the coupling between NAO and decadal MOC variability. The present model emphasizes excitation by NAO-induced wind fluctuations. This results in a fast response to NAO fluctuations, with a lag of 1 yr.

In addition we show the pattern and amplitude of the intra-annual variability (Fig. 6). Here, the amplitude is

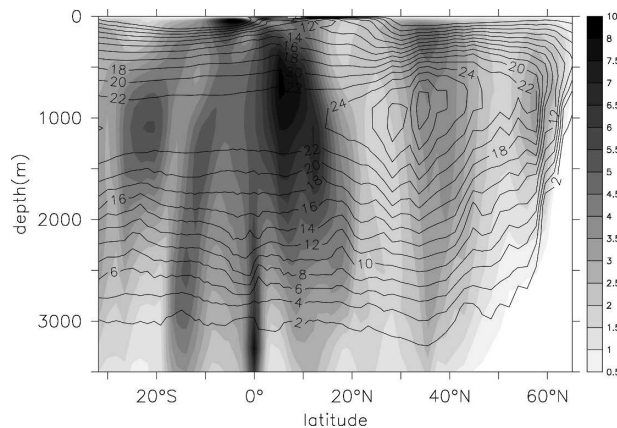


FIG. 6. Pattern of intra-annual variability of the MOC. This pattern is obtained by averaging the (square root of) the variance of each monthly mean value for the MOC with respect to the pertinent annual mean. Units are Sv.

much larger with peaks in tropical regions of 8–10 Sv. Highest peaks are found at 10°N at 500-m depth and in the Southern Hemispheric subtropical cell, just below the surface. A secondary maximum is found at 40°N at 250-m depth where the intra-annual variability attains amplitudes of 4 Sv. A region with relatively low values occurs between 20° and 30°N where the intra-annual variability does not exceed the 2 Sv. In general, the intra-annual variability of the MOC is much larger than its interannual variability, suggesting that without sustained measurements, in which the intra-annual variability can be averaged, detection of a MOC change is severely hampered.

5. Detection of MOC change

a. Method

In the previous sections we determined the signal and noise patterns for the MOC. In the present section we describe a method to detect this signal in the presence of such noise. Our detection method will be based on the associated signal-to-noise ratios. The model produces a continuous time series of monthly mean MOC values that can exactly be estimated at each point in space. This clearly represents an idealized situation that would never occur in reality. In the ideal “model world” the effect of observation error, infrequent observation, and the local character of observations, that is, typically a hydrographic section or mooring array, is absent. To illustrate the method of detecting MOC changes we start to estimate signal-to-noise ratios for the ideal “model world.” Thereafter, we extend our diagnosis to include an estimate of the observation error.

The ensemble experiment allows us to construct a full two-dimensional picture of the signal-to-noise ratio for the Atlantic MOC. All simulations start in 1950 and stop in 2080. For each moment between 1950 and 2080, we can estimate the signal from the linear trend in ensemble-mean MOC year t and 1950, multiplied by the length of the “observation period”: $t-1950$. Also, we can estimate the ensemble-mean variance from the anomalous MOC, as defined with respect to the ensemble-mean MOC (as a function of time), for each individual member. The signal-to-noise ratio R then becomes

$$R = \frac{\alpha(t)(t - t_0)}{\sqrt{\sigma_i(t)^2}}, \quad (1)$$

where $\alpha(t)$ is defined as the linear trend in MOC between year t and year t_0 ; t_0 is 1950, the starting date of the experiment; σ_i is the average interannual variability for the period t_0 to t .

However, each model drifts. In most cases, the signal that we want to detect should exclude the drift. In these cases we might use a certain initial period, say 1950–60, to estimate the drift by calculating the linear trend over this period. Then, the signal at each moment $t > 1960$ is defined by the difference in linear trends over the periods 1950– t and 1950–1960, multiplied by the length of the time period: $t-1950$:

$$R = \frac{[\alpha(t) - \alpha(t_i)](t - t_0)}{\sqrt{\sigma_i(t)^2}}, \quad (2)$$

where t_i is defined as the end date of the period that is used to determine the initial model drift; that is, $t_i = 1960$. If we would have estimated signal-to-noise ratios for temperature or salinity, such a drift correction would have been obligatory. Drift in the MOC, however, is small and incoherent: $\alpha(t_i)$ is negligible and the signal-to-noise ratio for periods after 1960 is hardly affected by a correction for the initial drift. Therefore we have omitted the drift correction for the MOC.

b. Signal-to-noise ratio

Figure 7a shows the signal-to-noise ratio in the idealized model world at year 2005, assuming continuous measurements from 1950 onward. Because of continuous observation, MOC values have been annually averaged, which greatly reduces the noise. To yield a statistically significant detection with 95% reliability (assuming a Gaussian distribution) the signal-to-noise ratio should become larger than 1.9. From Fig. 7a we see that after 55 years of continuously monitoring the signal has become detectable in year 2005. However, at

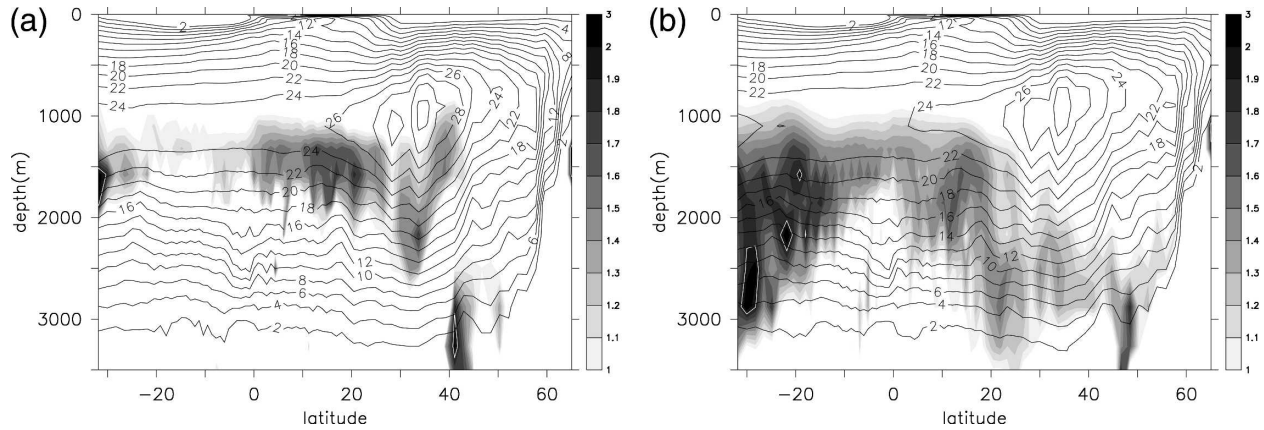


FIG. 7. (a) Signal-to-noise ratio for the ensemble-mean MOC change between 1950 and 2005 for annually averaged values. This figure is obtained by dividing the linear trend in MOC change for the first 55 years of the integration period, multiplied by the length of that period (55 yr), by the averaged square root of the (interannual) variance of that period. The 1.9 contour, associated with detection with 95% reliability, is contoured in white. The pattern is overlaid by contours of ensemble-mean overturning for the first 55 yr. (b) As in (a), but for the period between 2000 and 2020.

this stage detection is only possible at a few places. The most important one is at 30°S between 1500-m and 2000-m depth and at 40°N below 3000 m. Since the latter maximum is associated with both a weak signal and weak noise (but a high signal-to-noise ratio), it is disregarded. A third, yet not statistically significant, maximum occurs between 0° and 25°N around a depth of 1500 m. This is a region with a large signal, but also high noise levels. The overall depth level at which the signal-to-noise ratio peaks is found at about 1500 m.

Both signal and noise display maxima near 35°N; see Figs. 2 and 3. The signal pattern, however, is much broader in latitudinal extent than the noise pattern. Although the signal pattern shown in Fig. 2 refers to a later period (2000–80), the general characteristics of the signal pattern are robust with time. For the 1950–2000 period, the trend is weaker by a factor of 3 with maximum amplitudes at shallower depths: 1500 versus 2000 m. Also, the pattern is more confined to the Northern Hemisphere midlatitudes. Apparently, the MOC reduction starts in the region where the maximum overturning occurs. In a later phase the whole MOC shoals and its reduction attains a more global character.

If we would have started continuous monitoring in year 2000, detection of the MOC decrease would have occurred much faster than if the starting date had been 1950. Detection now occurs after 20 years of monitoring because the negative trend in the MOC increases from 1950 to 2000. After 2000, the MOC trend no longer increases. It equilibrates at the value determined by the GHG forcing. Figure 7b shows the signal-to-noise ratio for the period 2000–20. Comparing with Fig. 7a we see that the signal-to-noise pattern is broadened,

consistent with a more global pattern of MOC decrease after 2000. Also, it is slightly shifted to greater depths, associated with the onset of the shoaling of the MOC.

If we would not be able to continuously monitor the MOC, but would have to estimate the meridional mass transport on an intermittent basis, the noise estimate has to include the intra-annual variability, which significantly enhances the noise level:

$$R = \frac{\alpha(t)(t - t_0)}{\sqrt{\sigma_i(t)^2 + \sigma_m(t)^2}}, \quad (3)$$

where σ_m^2 is the intra-annual (monthly) variability. The pattern of the intra-annual variability is broad, with a maximum at the equator where the noise level is 10 Sv, decaying to 4 Sv at the midlatitudes. When the noise includes intra-annual variability, and starting with a first estimate in 1950, detection becomes possible in 2035, that is, after 85 instead of 55 years; see Fig. 8a. Owing to the overall increase of the noise level, the signal-to-noise pattern now more strongly emphasizes regions where the signal pattern displays a maximum. Detection first becomes possible between 20° and 30°N at depths between 1500 and 2500 m. A second maximum occurs at 50°N at a depth of about 3000 m. Here both signal and noise are weak and the high signal-to-noise ratio will not be robust for slight increases of the noise level. If the first estimate of the MOC were made in year 2000 instead of 1950, the moment of detection would come slightly later: in year 2045. The signal-to-noise pattern for the period 2000–45 is quite similar to the pattern for the period 1950–2035; compare Figs. 8a and 8b. Note that, starting observations in 2000, the

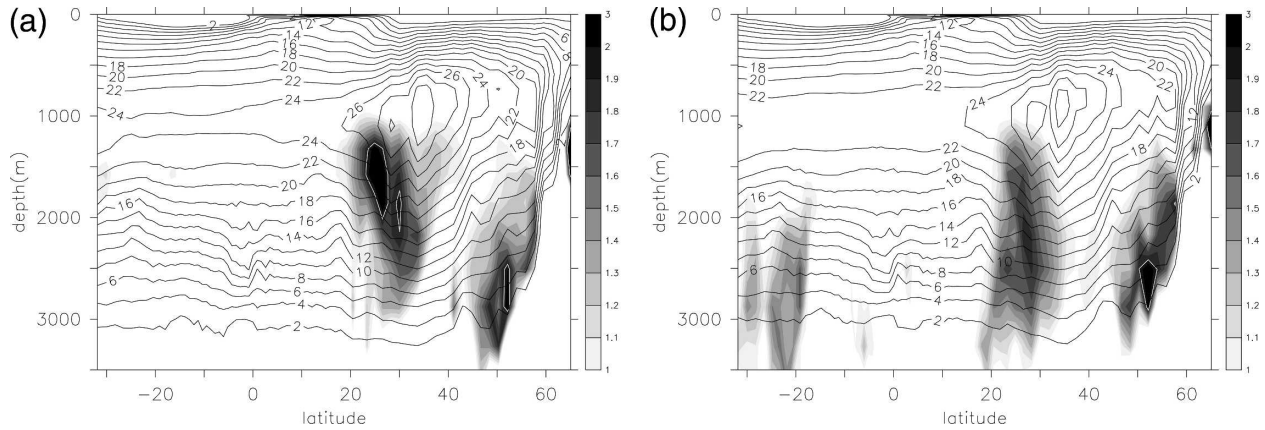


FIG. 8. (a) Signal-to-noise ratio for the period 1950–2035 after adding intra-annual variations to the noise estimate. (b) As in (a), but for the period 2000–45.

time needed to detect a trend in the MOC, when the MOC is only episodically estimated, increases from 20 to 45 years. This increase with a factor of 2.25 is solely due to the large increase of the noise level when intra-annual variability has to be accounted for.

Until now detection occurred in the “ideal world” of a model, without any observation error. Error estimation for mass transports across a hydrographic section is complicated and inevitably crude. Ganachaud (2003) estimated the various error sources for an inverse box model. The most important error appears to be associated with internal waves. Internal waves move isopycnals in a nongeostrophic manner. So, the measured isopycnal positions deviate from their geostrophic positions. According to Ganachaud (2003) this error scales with f^{-1} , f being the Coriolis frequency, and with $\int_{-h}^0 N(z) dz$, where N is the local buoyancy frequency and h is the depth in the (y, z) plane. With the use of this scaling we have mapped the “internal wave error” for the whole (y, z) field of the MOC. At a latitude of 30°N and 4000-m depth, the error is 3 Sv. In addition, Ganachaud (2003) discussed an error due to the geostrophic assumption. He estimated this to be 2 Sv. We assume this error to possess an e -folding signature with depth, with a scale height of 500 m, and the top to bottom integral of the error to be 2 Sv. Also, this error is scaled with f^{-1} . Other errors are small and can be neglected. The noise estimate now includes the inter-annual and intra-annual variability and an observational error as described above:

$$R = \frac{\alpha(t)(t - t_0)}{\sqrt{\sigma_i(t)^2 + \sigma_m(t)^2 + \epsilon^2}}, \quad (4)$$

where ϵ is the observational error. The resulting signal-to-noise pattern (Fig. 9a) is quite similar to the signal-

to-noise ratio from Fig. 8a, which excluded the observational error, but detection now occurs 20 years later in 2055.

If continuously monitoring is assumed, the error analysis of Ganachaud (2003) is no longer relevant. For instance, the “internal wave error” will be averaged out when constructing annual averages. For this particular error analysis we take as starting point the same monitoring design as discussed by Hirschi et al. (2003) and Baehr et al. (2004). The error associated with the geostrophic assumption can be reduced if cable measurements or current meter estimates are used for the western boundary current. The error in such measurements typically is 1 Sv. On the basis of Fig. 3 in Hirschi et al. (2003) we estimate the error associated with the geostrophic estimate to be 0.5 Sv, which we scale with f^{-1} . Figure 9b shows the signal-to-noise ratio in year 2035, after continuous monitoring started in year 2000. Detection now has become possible after 35 years of sustained observations. The detection time (35 yr) has significantly increased compared to the estimate, which does not include the observation error (20 yr), but it is much shorter than the detection time based on snapshots, even if no observation error is assumed in that case (45 yr). The pattern of Fig. 9b displays two maxima, one around 25°S and another around 20°N; both occur at a depth of 2000 m. The probability of detection is slightly larger at 25°S than at 20°N because the interannual noise level is lower there.

c. Detection times

Until now we constructed the signal-to-noise ratio from the signal and noise within a certain time slice in which measurements of the MOC were taken. A more robust estimate of the signal-to-noise ratio of the MOC

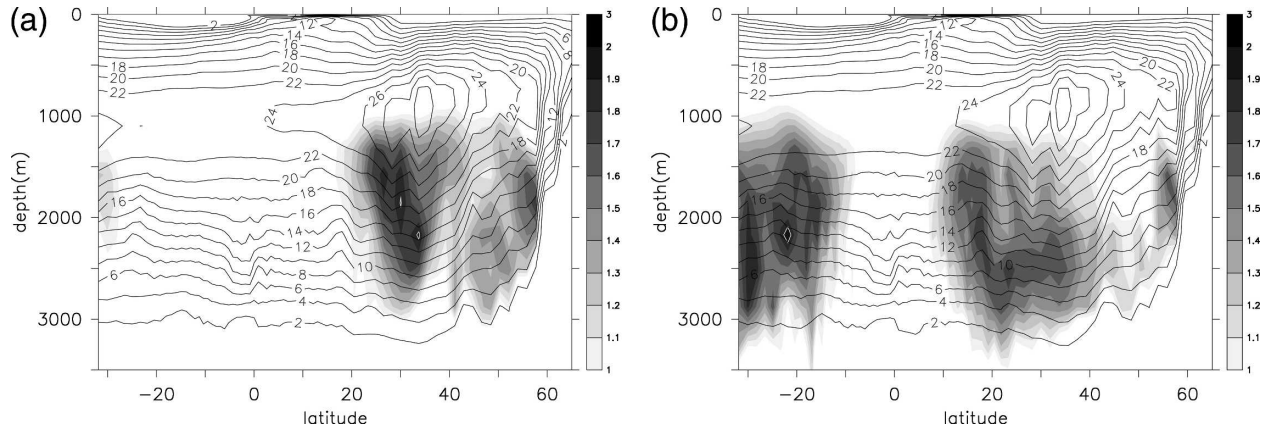


FIG. 9. (a) Signal-to-noise ratio for the period 1950–2055 after adding an observation error to the noise estimate based on snapshot measurements. (b) Signal-to-noise ratio for the period 2000–35 after adding an observation error to the noise estimate based on sustained measurements.

can be constructed when the signal and noise over the whole 2000–80 period (or 1950–2080 period) is taken into account. Both signal and noise display some decadal variability that modulates the signal-to-noise ratio. This modulation is minimized when the whole 2000–80 period is considered. Assuming that detection capability occurs when the signal-to-noise ratio R becomes larger than 1.9, the detection time T becomes

$$T = 1.9\Delta\tau/R, \quad (5)$$

where $\Delta\tau = 80$ yr, being the period over which the signal-to-noise ratio is estimated. When this formula for the detection time is used, it is implicitly assumed that both signal and noise remain (almost) constant over the period 2000–80. In this period both signal and noise indeed are almost stationary. There are some changes in the interannual variability over this period, but these changes only affect detection times that fall beyond the 2000–80 interval, which are not of interest here. In Fig. 10 the estimated detection time is shown, defined to be the time, starting in year 2000, to reach a signal-to-noise ratio of 1.9. Two large regions appear that possess detection times less than 40 yr. The largest area is between 10° and 40°N at about a depth of 2000 m. The second large area is between 30° and 20°S , also at 2000-m depth. This figure confirms the rationale for the U.K./U.S. RAPID/WAVE monitoring array design at 26°N (see Hirschi et al. 2003; Baehr et al. 2004). At the same time it suggests that, if a second monitoring array would be considered, it would be most fruitful to deploy such a system near 25°S , just north of the eddy-rich area in the Cape Basin.

A summary of these findings is given in Fig. 11. This figure shows the signal-to-noise ratio for the MOC at 26°N and a depth of 2000 m as a function of time, based

on sustained measurements (starting in 2000 and 2019) and based on snapshot measurements (starting in 1950 and 2000), respectively. The signal and noise was estimated for the periods 1950–2000 and 2000–80 separately. Figure 11 shows that detection of a MOC change based on sustained measurements that have started in 2000 occurs in 2036. Detection based on snapshot measurements starting in 1950 occurs in 2055. The same moment of detection occurs for sustained measurements starting in 2019. When only snapshot measurements of the MOC are available from year 2000 and later, detection will not occur before 2080.

6. Discussion

The signal-to-noise ratio that we calculate bears some similarity with the fingerprint method advocated

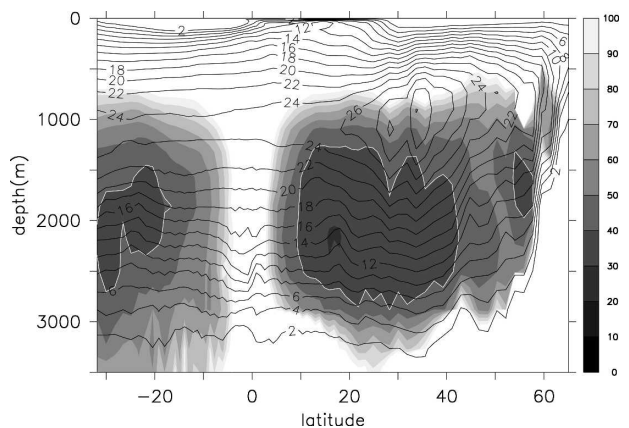


FIG. 10. Detection time, in years, based on the linear trend in MOC change between 2000 and 2080 and assuming continuous monitoring. The noise estimate excludes intra-annual variability, but includes an observation error. The 40-yr detection time contour is highlighted in white.

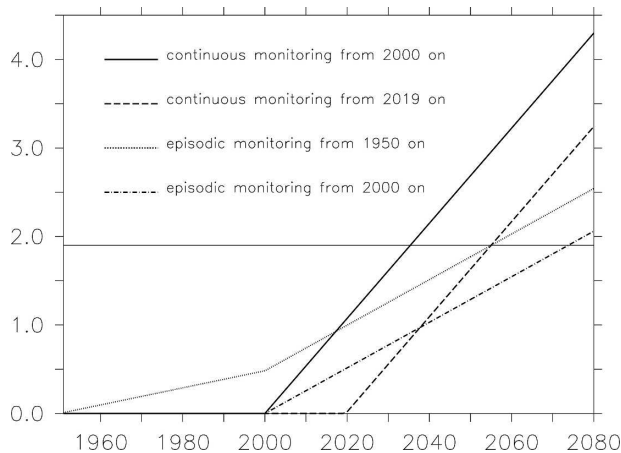


FIG. 11. The signal-to-noise ratio at 26°N and a depth of 2000 m as a function of time. Estimates are based on sustained measurements starting in 2000 (straight line) and 2019 (dashed line) and on snapshot measurements starting in 1950 (dotted line) and 2000 (dash-dot line), respectively. The thin straight line marks the signal-to-noise ratio of 1.9 where detection becomes possible.

by, for example, Hasselman (1993) and Hegerl et al. (1996). Our signal pattern can be compared to the guess pattern in the fingerprint method; the fingerprint itself can be constructed from the (inverse of the) detection time shown in Fig. 10. The (optimal) fingerprint method itself uses slightly more sophisticated methods to estimate the final fingerprint signal, but as a complete two-dimensional reconstruction of the MOC from observations is not likely to become possible in the near future, the construction of such an optimal fingerprint for the MOC does not seem to be pertinent. The main motivation for calculating signal-to-noise ratios and detection time, as shown in Fig. 10, is that it is useful for local monitoring strategies and detection methods.

The time at which a MOC decrease can be inferred from episodal measurements has been estimated to be around 2055. This would imply that the strong slowing of the MOC, as reported by Bryden et al. (2005), is for a large part due to a change that must be associated with internal, mostly intra-annual variability. On the other hand, it could very well be that in nature the MOC is subject to a GHG-forced signal that is much stronger than any model has been able to simulate so far (Gregory et al. 2005; Schmittner et al. 2005). Bryden et al. (2005) suggest that the observed change is due to a “real” signal, although the change is very close to the error estimate, because the observed change is almost exclusively associated with a decrease of southward flow between 3000 and 5000 m, consistent with a decrease in NADW formation. Our results also indicate that a GHG-forced MOC change will be most significant at 2000–3000-m depth, as the NADW outflow will

shift to shallower depths and the deepest branch of NADW outflow is subject to largest decline. So, Bryden et al. (2005) observe a change where we expect the signal to be strongest, but the amplitude of the noise is still too high to make any firm conclusions.

We are aware that we reach these conclusions with a large ensemble of climate scenario runs made with a coarse-resolution climate model, in particular a model with a strong bias in mean MOC toward too high overturning values. On the other hand, the pattern and amplitude of the GHG-forced signal and internal variability appear realistic compared to other models. But we recognize that higher-resolution models tend to show increased variability, in particular on longer decadal time scales (Bryan et al. 2006). Also, the simulations that we discuss use constant climate forcing after year 2000, except for the GHG emissions. This will reduce the ensemble-mean variability of the MOC, but might also affect its internal variability. As a result, the signal-to-noise ratios and detection times we calculate probably should be considered as lower boundary values. We are confident, however, that the patterns we show of the signal-to-noise ratio and detection time are not too model dependent, although the quantitative estimates may change when a more sophisticated climate model is used. In our view, the main thrust of this paper is the evaluation of the method to construct these patterns and their most important qualitative features.

7. Summary and conclusions

For an ensemble of greenhouse scenario runs we have shown the signal-to-noise patterns for the MOC, where the signal was defined as the linear trend in ensemble-mean MOC, and the internal variability was estimated from the variance in anomalous MOC (with respect to the ensemble-mean MOC) for each individual ensemble member. The GHG-forced signal consists of an overall decrease and shoaling of the MOC, with maximum amplitudes of about $10 \text{ Sv} (100 \text{ yr})^{-1}$. The maximum decrease is reached at 2000–3000-m depths. The maximum overturning itself decreases with 6 to $7 \text{ Sv} (100 \text{ yr})^{-1}$. Both pattern and amplitude compare well with other model estimates. The interannual variability of the MOC is dominated by a monopole with maximum amplitude of 2 Sv at the overturning maximum at 40°N . This natural variability has a three-dimensional character and is strongly correlated with the dominant mode of variability of the barotropic gyre. When this mode is regressed on atmospheric patterns, the NAO and its various imprints appears, suggesting that the NAO drives the North Atlantic Ocean variability. The regression between the NAO and MOC

variability peaks when the NAO leads by 1 yr, suggesting that the NAO mainly forces the MOC through wind variations.

The signal-to-noise ratio was estimated starting either in 1950 (the starting point of the analysis) or in 2000, when the linear GHG-forced trend has become stationary. Different noise estimates were made, both with and without intra-annual variability, relevant for episodic and continuous monitoring, respectively, and with and without an estimate of the observational error. When the observational error is included, detection of a GHG-forced MOC trend on the basis of episodic measurements appears impossible before 2055, assuming a first point measurement in 1950. With continuous monitoring, detection becomes possible after 35 years of observation. Shortest detection times occur between 10° and 40°N and between 1500-m and 3000-m depth, and between 20° and 35°S at the same depth levels. This confirms the rationale for the U.K./U.S. RAPID/WAVE monitoring array design at 26°N. At the same time it is suggested that a possible second monitoring array would be most efficiently deployed near 25°S.

Acknowledgments. Computer resources were funded by the National Computing Facilities Foundation (NCF). We thank Michael Klijhuis for technical support.

REFERENCES

- Baehr, J., J. Hirschi, J.-O. Beismann, and J. Marotzke, 2004: Monitoring the meridional overturning circulation in the North Atlantic: A model-based array design study. *J. Mar. Res.*, **62**, 283–312.
- , K. Keller, and J. Marotzke, 2007: Detecting potential changes in the meridional overturning circulation at 26°N in the Atlantic. *Climatic Change*, in press.
- Boville, B. A., J. T. Kiehl, P. J. Rasch, and F. O. Bryan, 2001: Improvements to the NCAR CSM-1 for transient climate simulations. *J. Climate*, **14**, 164–179.
- Bryan, F. O., G. Danabasoglu, N. Nakashiki, Y. Yoshida, D.-H. Kim, J. Tsutsui, and S. C. Doney, 2006: Response of the North Atlantic thermohaline circulation and ventilation to increased carbon dioxide in CCSM3. *J. Climate*, **19**, 2382–2397.
- Bryden, H. L., H. R. Longworth, and S. A. Cunningham, 2005: Slowing of the Atlantic meridional overturning circulation at 25°N. *Nature*, **438**, 655–657.
- Curry, R. G., and M. S. McCartney, 2001: Ocean gyre circulation changes associated with the North Atlantic Oscillation. *J. Phys. Oceanogr.*, **31**, 3374–3400.
- Dai, A., T. M. L. Wigley, B. A. Boville, J. T. Kiehl, and L. E. Buja, 2001: Climates of the twentieth and twenty-first centuries simulated by the NCAR Climate System Model. *J. Climate*, **14**, 485–519.
- Delworth, T. L., and R. J. Greatbatch, 2000: Multidecadal thermohaline circulation variability driven by atmospheric surface flux forcing. *J. Climate*, **13**, 1481–1495.
- , S. Manabe, and R. J. Stouffer, 1993: Interdecadal variations of the thermohaline circulation in a coupled ocean–atmosphere model. *J. Climate*, **6**, 1993–2011.
- Dijkstra, H. A., and M. Ghil, 2005: Low-frequency variability of the large-scale ocean circulation: A dynamical systems approach. *Rev. Geophys.*, **43**, RG3002, doi:10.1029/2002RG000122.
- Dixon, K., T. Delworth, M. Spelman, and R. Stouffer, 1999: The influence of transient surface fluxes on North Atlantic overturning in a coupled GCM climate change experiment. *Geophys. Res. Lett.*, **26**, 2749–2752.
- Dong, B. W., and R. T. Sutton, 2001: The dominant mechanisms of variability in Atlantic Ocean heat transport in a coupled GCM. *Geophys. Res. Lett.*, **28**, 2445–2448.
- Drijfhout, S. S., and W. Hazeleger, 2006: Changes in MOC and gyre-induced Atlantic Ocean heat transport. *Geophys. Res. Lett.*, **33**, L07707, doi:10.1029/2006GL025807.
- Eden, C., and J. Willebrand, 2001: Mechanism of interannual to decadal variability of the North Atlantic circulation. *J. Climate*, **14**, 2266–2280.
- Ganachaud, A., 2003: Error budget of inverse box models: The North Atlantic. *J. Atmos. Oceanic Technol.*, **20**, 1641–1655.
- , and C. Wunsch, 2000: Improved estimates of global ocean circulation, heat transport and mixing from hydrographic data. *Nature*, **408**, 453–457.
- Gent, P. R., and J. C. McWilliams, 1990: Isopycnal mixing in ocean circulation models. *J. Phys. Oceanogr.*, **20**, 150–155.
- Gregory, J. M., and Coauthors, 2005: A model intercomparison of changes in the Atlantic thermohaline circulation in response to increasing atmospheric CO₂ concentration. *Geophys. Res. Lett.*, **32**, L12703, doi:10.1029/2005GL023209.
- Hasselmann, K., 1993: Optimal fingerprints for the detection of time-dependent climate change. *J. Climate*, **6**, 1957–1971.
- Hegerl, G. C., H. von Storch, K. Hasselmann, U. Cubasch, B. D. Santer, and P. D. Jones, 1996: Detecting anthropogenic climate change with an optimal fingerprint method. *J. Climate*, **9**, 2281–2306.
- Hirschi, J., J. Baehr, J. Marotzke, J. Stark, S. Cunningham, and J.-O. Beismann, 2003: A monitoring design for the Atlantic meridional overturning circulation. *Geophys. Res. Lett.*, **30**, 1413, doi:10.1029/2002GL016776.
- Johnson, H. L., and D. P. Marshall, 2002: A theory for the surface Atlantic response to thermohaline variability. *J. Phys. Oceanogr.*, **32**, 1121–1132.
- Latif, M., E. Roeckner, U. Mikolajewicz, and R. Voss, 2000: Tropical stabilization of the thermohaline circulation in a greenhouse warming simulation. *J. Climate*, **13**, 1809–1813.
- Manabe, S., and R. J. Stouffer, 1988: Two stable equilibria of a coupled ocean–atmosphere model. *J. Climate*, **1**, 841–866.
- , and —, 1994: Multiple century response of a coupled ocean–atmosphere model to an increase of atmospheric carbon dioxide. *J. Climate*, **7**, 5–23.
- , and —, 1999: The role of the thermohaline circulation in climate. *Tellus*, **51**, 91–109.
- Mikolajewicz, U., and E. Maier-Reimer, 1994: Mixed boundary conditions in ocean general circulation models, and their influence on the stability of the model’s conveyor belt. *J. Geophys. Res.*, **99**, 22 633–22 644.
- , and R. Voss, 2000: The role of the individual air–sea flux components in CO₂-induced changes of the ocean’s circulation and climate. *Climate Dyn.*, **16**, 627–642.
- Pardaens, A. K., H. T. Banks, J. M. Gregory, and P. R. Rowntree,

- 2003: Freshwater transports in HadCM3. *Climate Dyn.*, **21**, 177–195.
- Rahmstorf, S., 1995: Bifurcations of the Atlantic thermohaline circulation in response to changes in the hydrological cycle. *Nature*, **378**, 145–149.
- , and Coauthors, 2005: Thermohaline circulation hysteresis: A model intercomparison. *Geophys. Res. Lett.*, **32**, L23605, doi:10.1029/2005GL023655.
- Schmittner, A., M. Latif, and B. Schneider, 2005: Model projections of the North Atlantic thermohaline circulation for the 21st century assessed by observations. *Geophys. Res. Lett.*, **32**, L04602, doi:10.1029/2004GL022112.
- Selten, F. M., G. W. Branstator, H. A. Dijkstra, and M. Kliphuis, 2004: Tropical origins for recent and future Northern Hemisphere climate change. *Geophys. Res. Lett.*, **31**, L21205, doi:10.1029/2004GL020739.
- Stommel, H., 1961: Thermohaline convection with two stable regimes of flow. *Tellus*, **13**, 224–230.
- Thorpe, R. B., J. M. Gregory, T. C. Johns, R. A. Wood, and J. F. B. Mitchell, 2001: Mechanisms determining the Atlantic thermohaline circulation response to greenhouse gas forcing in a non-flux-adjusted coupled climate model. *J. Climate*, **14**, 3102–3116.
- Timmermann, A., M. Latif, R. Voss, and A. Grötzner, 1998: Northern Hemisphere interdecadal variability: A coupled air/sea mode. *J. Climate*, **11**, 1906–1931.
- Vellinga, M., and R. A. Wood, 2002: Global climatic impacts of a collapse of the Atlantic thermohaline circulation. *Climatic Change*, **54**, 251–267.
- Wood, R. A., A. B. Keen, J. F. B. Mitchell, and J. M. Gregory, 1999: Changing spatial structure of the thermohaline circulation in response to atmospheric CO_2 forcing in a climate model. *Nature*, **399**, 572–575.
- Wunsch, C., 2002: What is the thermohaline circulation? *Science*, **298**, 1180–1181.
- , and P. Heimbach, 2006: Estimated decadal changes in the North Atlantic meridional overturning circulation and heat flux 1993–2004. *J. Phys. Oceanogr.*, **36**, 2012–2024.